Lawrence Berkeley National Laboratory

Title

Visualizing functional dynamicity in the DNA-dependent protein kinase holoenzyme DNA-PK complex by integrating SAXS with cryo-EM

Permalink

https://escholarship.org/uc/item/9kv9z79k

Authors

Hammel, Michal

Rosenberg, Daniel J

Bierma, Jan

et al.

Peer reviewed
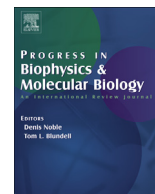
Visualizing functional dynamicity in the DNA-dependent protein kinase holoenzyme DNA-PK complex by integrating SAXS with cryo-EM

Michal Hammel [a, *], Daniel J. Rosenberg [a, b], Jan Bierma [a], Gregory L. Hura [a], Roopa Thapar [d], Susan P. Lees-Miller [c], John A. Tainer [d, **]

[a] Molecular Biophysics and Integrated Bioimaging, Lawrence Berkeley National Laboratory, Berkeley, CA, 94720, USA
[b] Graduate Group in Biophysics, University of California, Berkeley, CA, 94720, USA
[c] Department of Biochemistry and Molecular Biology, University of Calgary, Alberta, T2N 4N1, Canada
[d] Department of Cancer Biology, Department of Molecular and Cellular Oncology, University of Texas MD Anderson Cancer Center, Houston, TX, 77030, USA

ABSTRACT

Assembly of KU and DNA-dependent protein kinase catalytic subunit (DNA-PKcs) at DNA double strand breaks (DSBs) forms DNA-PK holoenzyme as a critical initiating step for non-homologous end joining (NHEJ) repair of DSBs produced by radiation and chemotherapies. Advanced cryo-electron microscopy (cryo-EM) imaging together with breakthrough macromolecular X-ray crystal (MX) structures of KU and DNA-PKcs recently enabled visualization of the ~600 kDa DNA-PK assembly at near atomic resolution. These important static structures provide the foundation for definition and interpretation of functional movements crucial to mechanistic understanding that can be tested through solution state structure analysis. We herein therefore leverage Cryo-EM and MX structures for the interpretation of synchrotron small-angle X-ray scattering (SAXS) data on DNA-PK conformations in solution to inform the structural mechanism for NHEJ initiation. SAXS, which measures thermodynamic solution-state conformational states and assemblies outside of cryo- and solid-state conditions, unveils the inherent flexibility of KU, DNA-PKcs and DNA-PK. The combined structural measurements reveal mobility of KU80 C-terminal region (KU80CTR), motion/plasticity of HEAT (DNA-PKcs Huntingtin, Elongation Factor 3, PP2 A, and TOR1) regions, allosteric switching upon DNA-PKcs autophosphorylation, and dimeric arrangements of DNA-PK assembly. Importantly, the results uncover displacement of the N-terminal HEAT domain during autophosphorylation as suitable for a regulated release mechanism of DNA-PKcs from DNA-PK to control unproductive access to toxic and mutagenic DNA repair intermediates. These integrated analyses show that the marriage of SAXS with cryo-EM leverages the strengths of both techniques to enable assessment of functional conformations and flexibility defining atomic-resolution molecular mechanisms for DSB repair.

1. Introduction

A major enabling step in understanding non-homologous end joining (NHEJ) DNA repair has been realized through breakthrough comprehensive and high-resolution visualizations of DNA-PKcs by combining cryo-EM (Sharif et al., 2017; Baretic et al., 2019) with X-ray crystallographic (Sibanda et al., 2017) results. Defining the structural mechanisms for NHEJ are important for cancer etiology and therapeutic strategies since this is the primary DSB repair pathway in humans. Alternative DSB repair pathways either involve homology-directed repair or the more error prone alternative end joining that depends upon XRCC1 complexes (Eckelmann et al., 2020; Dutta et al., 2017; Lafrance-Vanasse et al., 2015; Syed and Tainer, 2018). To obtain structural insights before the current cryo-EM structures, it was necessary to build up models of the NHEJ complexes one component at a time (Williams et al., 2014). Importantly, such insights pertain to genome instability seen in some

---

cancers associated with translocations that depend upon the actions of NHEJ proteins and that are particularly associated with non-B DNA-forming sequences (Ghezraoui et al., 2014; Bacolla et al., 2016). Moreover, as DNA-PK has functional interactions with poly(ADP-ribose) polymerase (PARP1) (Spagnolo et al., 2012) and both PARP1 and poly(ADP-ribose) glycohydrolase (PARG) inhibitors are actively being pursued for targeting the DNA damage response to kill cancer cells, these DNA-PK complexes are certainly relevant to ongoing cancer research (Bryant et al., 2005; Houl et al., 2019).

Currently, in cases where cryo-EM provided only near atomic resolution, integration of high-resolution crystal structures of the assembly and components (Sibanda et al., 2017; Walker et al., 2001) into the cryo-EM maps enabled the reconstruction of atomistic models for the larger KU-DNA-DNA-PKcs (DNA-PK) assembly (Yin et al., 2017). Yet, these are flexible complexes. In order to create a tractable sample for cryo-EM analysis, crosslinking agents were required to stabilize the complex. Such crosslinking limits assessment of flexibility but implies the complex is functionally dynamic. Indeed, the complex is expected to undergo allosteric transitions for function. We have therefore been developing and applying solution state small angle X-ray scattering (SAXS) techniques to complement cryo-EM and X-ray crystallographic structures, bridge size restrictions on techniques and provide a perspective on functionally-relevant solution behavior.

Previously we employed SAXS data to evolve understanding of static structures into dynamic multi-state functional conformations and to visualize flexible or unfolded regions (Hammel, 2012; Putnam et al., 2007; Brosey and Tainer, 2019; Hura et al., 2013). Due to rotational averaging, the information content of SAXS is dramatically reduced compared to a density maps generated from cryo-EM or crystallography. Two advantages of SAXS, however, are that it provides objective data on flexibility (Rambo and Tainer, 2011) and that SAXS profiles can be efficiently calculated from atomistic models and directly matched to experimental data (Schneidman-Duhovny and Hammel, 2018). As a result, multi-state data-based models that mimic dynamic rearrangements, such as domain motions, transient complexation, and the presence of unfolded regions, can be robustly determined by SAXS-based atomistic modeling (Pelikan et al., 2009; Schneidman-Duhovny et al., 2016). Moreover, high-throughput SAXS data collection techniques, including size-exclusion, chromatography-coupled SAXS (SEC-SAXS) (Hura et al., 2009), enable the collection of many samples at multiple different conditions, facilitating the integration of SAXS with cryo-EM and crystallography (Knott et al., 2019; Horst et al., 2019; Hammel et al., 2010a). E.g. such SEC-SAXS unveiled the basis for the regulation of the cancer-important P53 protein (Zhou et al., 2019). Indeed, first defining and then controlling functional conformations by small molecules can control activities and even repair pathway choice as seen for the MRE11 complex (Lafrance-Vanasse et al., 2015; Shibata et al., 2014).

Here, we build upon published SAXS data and studies that characterized KU, KU-DNA, DNA-PKcs (Hammel et al., 2010a, 2016), and the DNA-PK assembly (Hammel et al., 2016) and incorporate newly available atomic structures. Integrating atomic structures/models with new approaches in SAXS-based atomistic modeling (Schneidman-Duhovny and Hammel, 2018; Schneidman-Duhovny et al., 2016; Panjkovich and Svergun, 2016) allowed us to derive dynamic models of the DNA-PK assembly and its components. From these analyses, we characterized a displacement of the KU80 C-Terminal Region (KU80CTR) from the KU core, show an inherent swing-like motion of the DNA-PKcs M and N- HEAT regions and identify a significant contraction of this N-HEAT region upon DNA-PKcs autophosphorylation. Interestingly, similar functional contractions and swing-like motions have been seen in the MRE11-RAD5O-NBS1 complex that acts in the homology-directed DSB repair as the major alternative pathway to NHEJ (Syed and Tainer,

2018; Kashammer et al., 2019). We moreover define and validate the solution state of the DNA-PK assembly that suggests stabilization of the DNA-PKcs HEAT regions upon recruitment to the KU-DNA complex. Intriguingly, we show that DNA-PKcs and DNA-PK can form a head to head interaction that appears to be a likely suitable precursor of the pre-synaptic NHEJ complex.

2. Materials and methods

2.1. Purification of proteins

DNA-PKcs and KU were purified from HeLa cells as described (Goodarzi and Lees-Miller, 2004; Chan et al., 1996). KUΔCTR (KU70/KU80 1—569) were expressed and purified from baculovirus-infected insect cells as described (Radhakrishnan and Lees-Miller, 2017). Large-scale preparations of phosphorylated DNA-PKcs for structural analysis were prepared as described by (Hammel et al., 2010a). 20-bp double-stranded DNA containing a short DNA stem-loop on one end for the preparation of KU-DNA complex was annealed and purified according (Hammel et al., 2010a). 20-bp double-stranded DNA containing a short DNA stem-loop on one end and a 5′-nucleotide (nt) overhang on the other for the preparation of the DNA-PK complex was annealed and purified according (Hammel et al., 2016).

2.2. SAXS experiment

For small-angle X-ray scattering coupled with multi-angle light scattering in line with size-exclusion chromatography (SEC-SAXS-MALS) experiments, 60 μL samples containing either 5 mg/mL of KUΔCTR and 5 mg/mL KU were prepared in 50 mM Hepes 7.5, 50 mM KCl, 5 mM MgCl$_2$, 5% glycerol and 0.2 mM DTT. SEC-SAXS-MALS were collected at the ALS beamline 12.3.1 LBNL Berkeley, California (Classen et al., 2013). X-ray wavelength was set at λ = 1.127 Å and the sample-to-detector distance was 2100 mm resulting in scattering vectors, q, ranging from 0.01 Å-1 to 0.4 Å-1. The scattering vector is defined as q = 4πsinθ/λ, where 2θ is the scattering angle. All experiments were performed at 20 °C (Dyer et al., 2014) and data was processed as described (Hura et al., 2009). Briefly, a SAXS flow cell was directly coupled with an online Agilent 1260 Infinity HPLC system using a Shodex KW803 column. The column was equilibrated with running buffer with a flow rate of 0.5 mL/min 55 μL of each sample was run through the SEC and 3 s X-ray exposures were collected continuously during a 30min elution. The SAXS frames recorded prior to the protein elution peak were used to subtract all other frames. The subtracted frames were investigated by the radius of gyration R$_g$ derived by the Guinier approximation I(q) = I(0) exp(-qR$_g$)^2/3 with the limits qR$_g$ < 1.5. The elution peak was mapped by comparing integral of ratios to background and R$_g$ relative to the recorded frame using the program SCÅTTER (Fig. S1). The eluent was subsequently split 3 to 1 between the SAXS line and a series of UV @ 280 and 260 nm, multi-angle light scattering (MALS), quasi-elastic light scattering (QELS), and refractometer detectors. MALS experiments were performed using an 18-angle DAWN HELEOS II light scattering detector connected in tandem to an Optilab refractive index concentration detector (Wyatt Technology). System normalization and calibration was performed with bovine serum albumin using a 45 μL sample at 10 mg/mL in the same SEC running buffer and a dn/dc value of 0.19. The light scattering experiments were used to perform analytical scale chromatographic separations for MW determination of the principle peaks in the SEC analysis. UV, MALS, and differential refractive index data was analyzed using Wyatt Astra 7 software to monitor the homogeneity of the sample across the elution peak complimentary to the above-mentioned SEC-SAXS signal validation (see Fig. S1).

The DNA-PKcs and KU-DNA-DNA-PKcs (DNA-PK) complex was prepared and measured by SEC-SAXS-MALS experiment (see Fig. 3A) as described by (Hammel et al., 2016). Additionally, SAXS data of KU, KU-DNA, DNA-PKcs, and phosphorylated DNA-PKcs were measured by high-throughput SAXS experiment (HT-SAXS) as described by (Hammel et al., 2010a). To improve the signal to noise ratio at higher q range SAXS curved derived from SEC-SAXS and HT-SAXS experiments were merged for KU and DNA-PKcs samples (see Figs. 1A and 2A, Table 1). DNA-PKcs in complex with 40-bp duplex with a Y-shaped structure at one end (DNA-PKcs-40bp Y-DNA) and 40bp DNA with the hairpin (40bp H-DNA) (Hammel et al., 2010a) and 40bp DNA with two blunt ends were measured by HT-SAXS as described by (Hammel et al., 2010a).

2.3. SAXS data evaluation

Final merged SAXS profiles where used for further analysis including Guinier plot which determined an aggregation free state (see Figs. 1A, 2A and 3B). The program SCÅTTER was used to compute the pair distribution function P(r). The distance r where P(r) approach zero intensity identifies the maximal dimension of the macromolecule (D_{max}). P(r) functions of KUΔCTR, KU, KU-DNA (Fig. 1B) and DNA-PK (Fig. 3C) were normalized based on the molecular weight of the assemblies as determined from SAXS curves by SCÅTTER using volume of correlation V_c (see Table 1) (Rambo and Tainer, 2013a, 2013b). To better visualized broadening of phosphorylated DNA-PKcs, the P(r) functions for DNA-PKcs and phosphorylated DNA-PKcs were
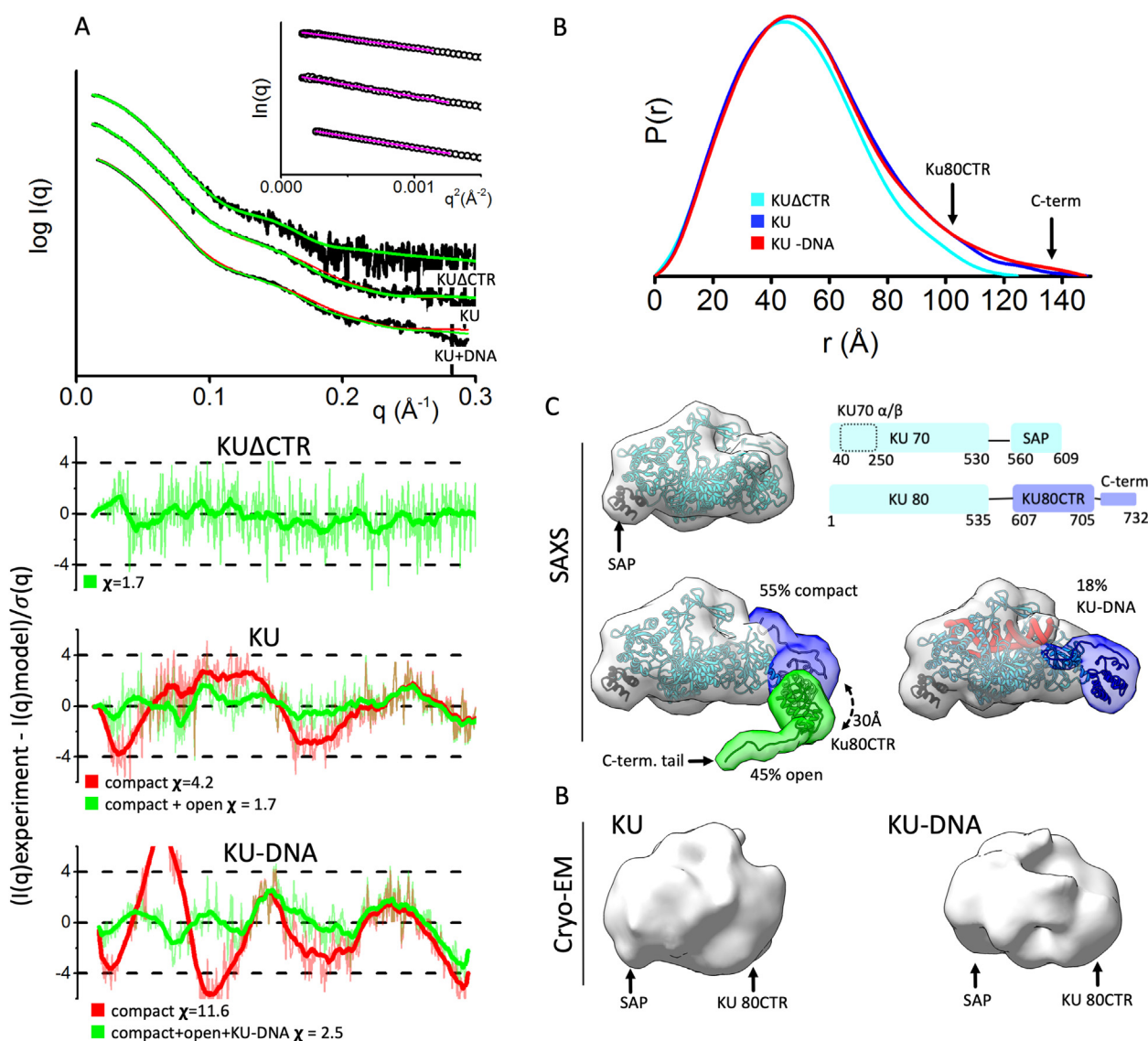

Fig. 1. KU80CTR is located in close proximity to the KU70 α/β region in DNA free and DNA bound states.
A) Experimental (black) and theoretical (colored as indicated) SAXS profiles for the solution state models of KUΔCTR, KU and KU-DNA. SAXS fits are shown together with the fit residuals and goodness of fit values (χ^2). Guinier plots for experimental SAXS curves are shown in inset.
B) Normalized pair distribution P(r) functions for experimental SAXS curves of KUΔCTR (cyan), KU (blue) and KU-DNA (red).
C) Top panel: Crystal structure of KU (Walker et al., 2001). A schematic representation highlighting the domains of KU: two KU70 regions composed of the KU core region and the SAP domain; and three KU80 regions composed of the KU80 core region, the KU80CTR domain and the KU80 C-terminal helix. Bottom panel: conformers in selected multi-state models of KU and KU-DNA used to calculate theoretical SAXS. The weight of each model is indicated. The two conformers (compact and open) used to fit experimental SAXS curves of KU and KU-DNA. The KU-DNA conformer with 18% weight is used independently. Atomistic models are displayed in ribbon style together with molecular envelop calculated at the 25 Å resolution to match the resolution of cryo-EM maps shown at the bottom panel.
D) cryo-EM maps of KU (EMD1270) and KU-DNA complex (EMD1271) (Rivera-Calzada et al., 2007).
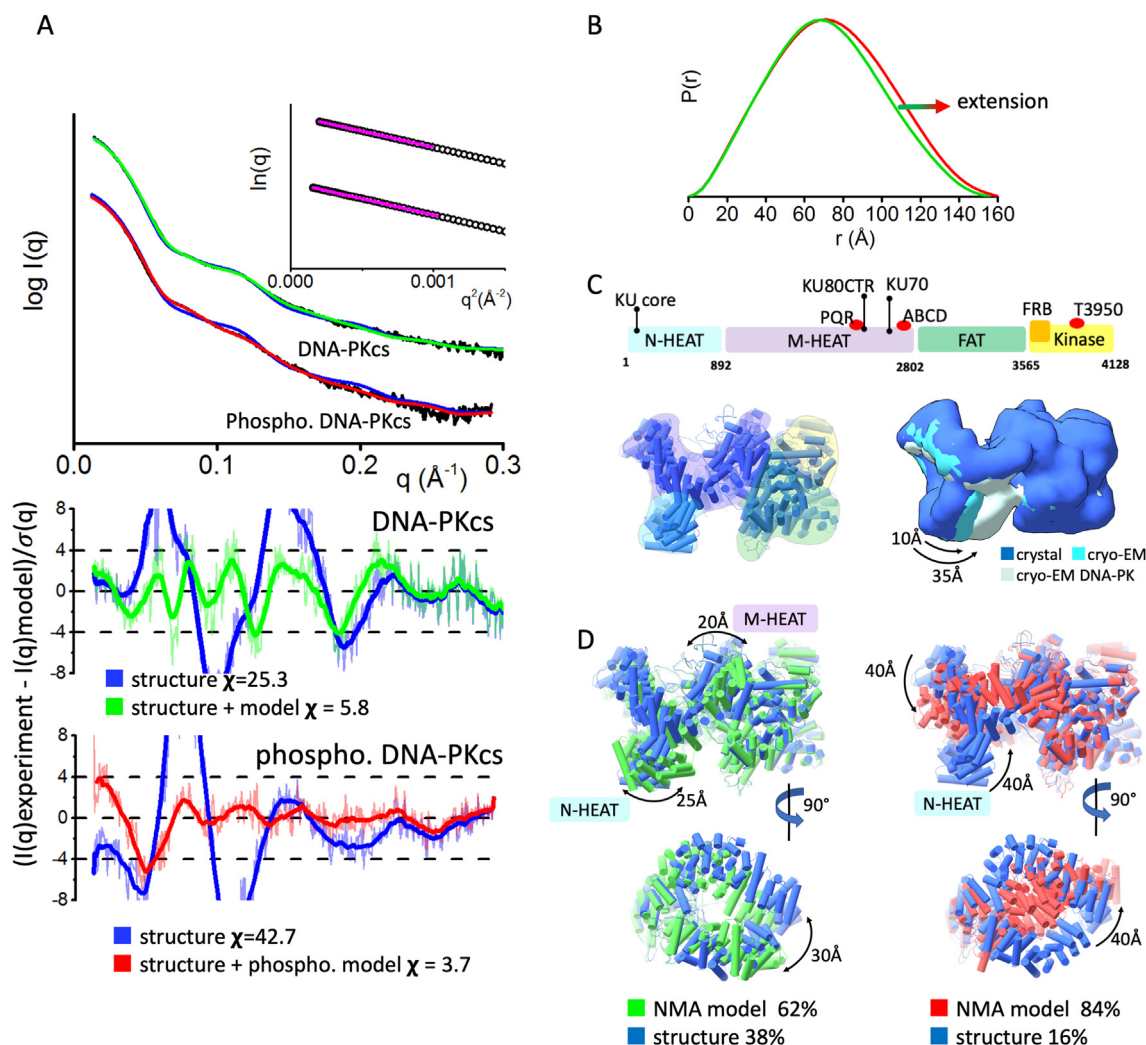
Fig. 2. Inherent dynamicity of DNA-PKcs HEAT region and its rearrangement during the autophosphorylation.
A) Experimental (black) and theoretical (colored as indicated) SAXS profiles for the solution state models of DNA-PKcs and autophosphorylated DNA-PKcs. SAXS fits are shown together with the fit residuals and goodness of fit values (χ^2). Guinier plots for experimental SAXS curves are shown in the inset.
B) Pair distribution P(r) functions, normalized at the maxima, for experimental SAXS curves of DNA-PKcs and autophosphorylated DNA-PKcs (taken from (Hammel et al., 2010a)).
C) Top panel: A schematic representation highlighting the four super secondary structural components of DNA-PKcs: the two HEAT region composed of the N-terminal domain (N-HEAT); the M-HEAT region and the Head regions, which contains the FAT and kinase regions. The KU binding area, FRB domain, autophosphorylation clusters PQR and ABCD, and highly conserved T3950 autophosphorylation site are shown above the schematic.
Left panel: Crystal structure of DNA-PKcs with highlighted N-HEAT, M-HEAT, FAT and kinase regions. middle panel: Comparison of the crystal structure and cryo-EM structure from (Sharif et al., 2017; Sibanda et al., 2017), and cryo-EM structure of DNA-PKcs taken from the DNA-PK complex (Yin et al., 2017). For better visualization of conformational variability in the HEAT region, atomic models are displayed as a molecular envelop at the 20 Å resolution.
D) Two orthogonal views of multistate model used to match experimental SAXS curves of DNA-PKcs and autophosphorylated DNA-PKcs. The models were superimposed on each other at the FAT region. The weight for each model is indicated.

normalized at their maxima (see Fig. 2B).

2.4. Solution structure modeling

The pool of KU conformers from our previous study (Hammel et al., 2010a) was used to fit the experimental SAXS curve of KU using FOXS (Schneidman-Duhovny et al., 2010, 2013, 2016) and a multi-state state model was selected using MultiFOXS (Schneidman-Duhovny et al., 2016) (see Fig. 1C). The same pool of conformers plus the pool of KU-DNA models from (Hammel et al., 2010a) was used to fit experimental SAXS of KU-DNA. A three-state model was selected by MultiFOXS (Schneidman-Duhovny et al., 2016) (see Fig. 1C).

To fit SAXS of DNA-PKcs and phosphorylated DNA-PKcs we initially built missing loops, including the ~2576−2776 region that contains the ABCDE phosphorylation sites (Douglas et al., 2002;

Ding et al., 2003) in to the X-ray crystal (Sibanda et al., 2017) and cryo-EM structures (Sharif et al., 2017) using MODELLER (Sali and Blundell, 1993). First we applied conformational sampling BIL-BOMD (Pelikan et al., 2009) to mimic the plasticity of the added loops. Next we optimized SAXS fit by large movement of DNA-PKcs domains using normal mode analysis (NMA) program SREFLEX (Panjkovich and Svergun, 2016). The SREFLEX program uses NMA in Cartesian space to estimate the flexibility of atomistic models to improve their agreement with experimental SAXS curve. The DNA-PKcs crystal structure (Sibanda et al., 2017) with added missing loops was divided into 4 regions that include residues 1−370 (N-terminal N-HEAT region), 371−1800 (N-HEAT and M-HEAT), 1801−2800 (second region of M-HEAT) and 2801−4119 (FAT and Kinase region). SREFLEX optimized the position of each domain relative to the others including normal mode elastic movement in

Table 1
Structural parameters from SAXS and MALS data.

SAXS sample SASBDB#	D_{max} (Å)	R_g (Å) from Guinier plot	R_g (Å) from P(r)	MW Seq. monomer (kDa)	MW SAXS (kDa)	MW MALS (kDa)	Model fit χ^2	data source
KUΔCTR SASDJV4	~125	37.9 ± 0.6	37.9	134	~140	145	1.7	SEC-SAXS (This study)
KU SASDJU4	~155	41.5 ± 1.4	42.7	153	~160	160	1.7	SEC-SAXS (This study) merged with SAXS from (Hammel et al., 2010a)
KU-DNA SASDJW4	~155	40.7 ± 0.3	41.9	173	~170	190	2.6	SAXS from (Hammel et al., 2010a)
DNA-PKcs SASDJX4	~155	57.1 ± 1.7	54.4	469	~480	480	5.9	SEC-SAXS from (Hammel et al., 2016) merged with SAXS from (Hammel et al., 2010a)
Autophospho. DNA-PKcs SASDJY4	~160	57.2 ± 1.7	56.0	469	~480	ND	3.7	SAXS from (Hammel et al., 2010a)
DNA-PK monomer SASDJZ4	~230	65.1 ± 0.6	66.8	640	~590	640	3.7	SEC-SAXS from (Hammel et al., 2016)
DNA-PK monomer/ dimer SASDJ25	~300	75.4 ± 1.5	83.5	640	~720	680−700	1.0	SEC-SAXS from (Hammel et al., 2016)
DNA-PKcs − 40bp DNA	~315	80.9 ± 4.2	92.9	499	~860	ND	1.8	SAXS from (Hammel et al., 2010a)
DNA-PKcs − 40bp H-DNA	~315	87.7 ± 6.3	96.4	497	~900	ND	1.3	SAXS from (Hammel et al., 2010a)
DNA-PKcs − 40bp Y-DNA	~315	90.2 ± 4.1	101.2	501	~880	ND	5.0	SAXS from (Hammel et al., 2010a)

the region. The generated 8 NMA models plus the crystal (Sibanda et al., 2017) and Cryo-EM (Sharif et al., 2017) structures (with added missing loops) is a pool of the models that were fitted to the experimental SAXS by FOXS (Schneidman-Duhovny et al., 2010, 2013, 2016) followed by selection of two-state model by MultiFOXS (Schneidman-Duhovny et al., 2016).

To fit the SAXS data of DNA-PKcs- 40-bp duplex with a Y-shaped structure at one end (40bp Y-DNA), 40bp DNA with the hairpin (40bp H-DNA) and 40bp DNA with two blunt ends (40bpDNA) we built atomistic model of DNA-PKcs dumbbell dimer by replacing KU in the DNA-PK structure (Yin et al., 2017) with DNA-PKcs (model 2). An alternative model with a different conformation of the N-HEAT 1−380 region was built by replacing DNA-PKcs with the conformers as seen in the crystal structure (model 1) (Fig. 3C). Due to conformational flexibility of the N-HEAT 1−380 region, DNA-PKcs may adopt a different tilt relative to the linear DNA (Fig. 3C). Thus alternative models with various tilts of DNA-PKcs were built (Model 3−9). We used the pool of the models that include dimer-models and DNA-PKcs monomer to fit the SAXS curve for all three DNA complexes using program FOXS (Schneidman-Duhovny et al., 2010, 2013, 2016), followed by selection of two-state model by MultiFOXS (Schneidman-Duhovny et al., 2016).

To fit the SAXS curve of the monomeric DNA-PK assembly we initially built missing loops in the cryo-EM structure (Yin et al., 2017) using MODELLER (Sali and Blundell, 1993). The missing KU80CTR domain was added in the close proximity of previously identify KU80CTR binding site at the M-HEAT region (Sibanda et al., 2017). DNA-PK model was fitted to the experimental SAXS data by FOXS (Schneidman-Duhovny et al., 2010, 2013, 2016).

To fit experimental SAXS curves of the DNA-PK monomer/dimer mixture we initially modeled a DNA-PKcs dimer by molecular docking of two DNA-PKcs monomers using a rigid docking, geometric shape-matching algorithm PatchDock (Schneidman-Duhovny et al., 2005). The docking of DNA-PKcs (taken from DNA-PK structure PDBID: 5Y3R (Yin et al., 2017)) was performed without symmetry operator. The docking of the DNA-PKcs crystal structure (Sibanda et al., 2017) (PDBID: 5ULQ) and SAXS-based atomistic model was performed with symmetry operator. The top

scoring model derived without symmetry operator resemble top scoring models with symmetry operator, and was further used to build the DNA-PK dimer model (Supplementary Fig. S2). DNA-PK dimers were constructed by aligning two DNA-PK monomers with the top scoring docking model of DNA-PKcs dimer. Experimental SAXS curve of DNA-PK monomer/dimer mixture was fitted by both monomer and dimer model using FOXS (Schneidman-Duhovny et al., 2010, 2013, 2016) followed by selection of two-state model by MultiFOXS (Schneidman-Duhovny et al., 2016).

Data and the related models were deposited in the SASBDB data base (https://www.sasbdb.org/). The SASBDB data base accession codes and experimental SAXS parameters are reported in Table 1.

3. Results

3.1. KU80 C-terminal region (CTR) dynamicity in DNA-free and DNA-bound states

Enhanced SAXS experiments and analysis identify and verify a preferentially close interaction between the flexibly linked KU80CTR domain and the main KU70 α/β domain. Analysis of SAXS data collected on statics samples assuming homogeneous monomers in solution had suggested the complete disassociation of KU80CTR relative to the KU core in both DNA-free and DNA-bound states (Hammel et al., 2010a). Our new measurements, obtained with size exclusion chromatography coupled with in-line SAXS and multiangle light scattering (SEC-SAXS-MALS, Fig. 1A, Supplementary Fig. S1), separated small amounts of transiently self-associating KU dimers, which had not been considered previously. Analyzing the SEC-SAXS from the monomeric peak demonstrated smaller radius of gyration (R_g) values and less elongated P(r) functions (Fig. 1B, Supplementary Fig. S1 and Table 1) than those observed in the static experiment (Hammel et al., 2010a). Further modelling through conformational sampling of the KU80CTR and KU80 C-terminal regions was applied (Pelikan et al., 2009) and, based on the goodness-of-fit (χ^2) between theoretical and experimental SAXS curves (Schneidman-Duhovny et al., 2013), the best single or multi-state models (Schneidman-Duhovny et al., 2016), were selected. The
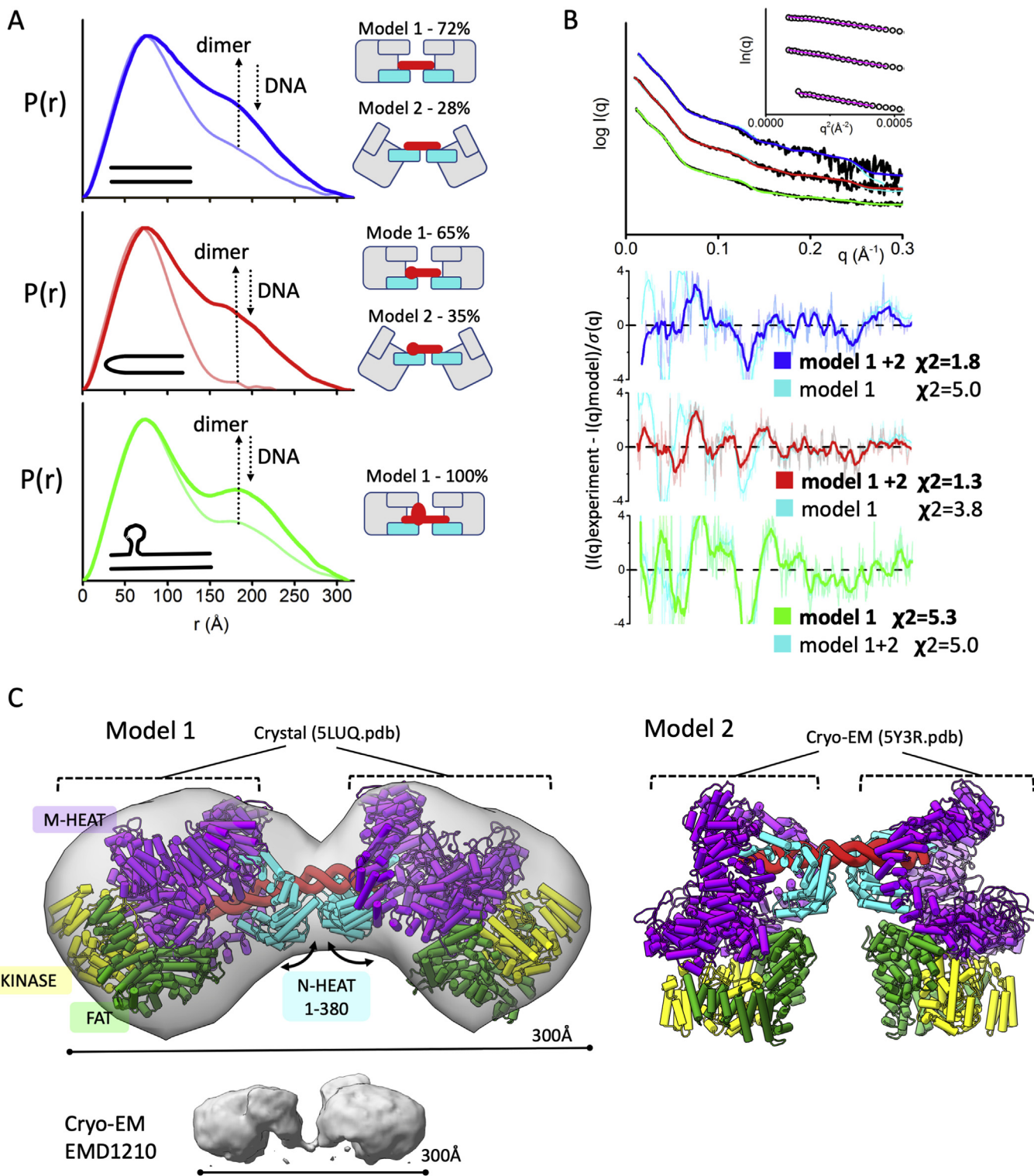
Fig. 3. Formation of dumbbell DNA-PKcs-DNA dimers

A) P(r) functions for DNA-PKcs - 40bp DNA (blue), 40bp H-DNA (red) and 40bp Y-DNA (green) with the ratio 2:1 (DNA-PKcs:DNA), calculated from the experimental SAXS shown in the panel B. The light-colored P(r) functions are shown for the samples with equimolar DNA-PKcs:DNA molar ratio. The left panel shows cartoon representations of the atomistic models and its weights for each DNA-PKcs-DNA complex that were used to match the SAXS data shown in the panel B.

B) Experimental (black) and theoretical SAXS profiles for the single (cyan) and multi-state model of DNA-PKcs in the complex with 40bp DNA (blue), 40bp H-DNA (red) and 40bp Y-DNA (green) with the DNA-PKcs:DNA ratio 2:1. SAXS fits are shown together with the fit residuals and goodness of fit values (χ^2). Guinier plots for experimental SAXS curves are shown in the inset.

C) Two atomistic models of DNA-PKcs dimer (model 1 and model 2) bridged by 40bpDNA (red). Model 2 was built based on the DNA-PK cryo-EM structure (Yin et al., 2017) by replacing KU with the DNA-PKcs. Model 1 was built by replacing both DNA-PKcs with DNA-PKcs-crystal structure (Sibanda et al., 2017). Conformational variability in the N-HEAT 1–380 region as seen between DNA-PKcs from DNA-PK (PDBID 5Y3R) and DNA-PKcs crystal structure (PDBID 5LUQ) results in altering of DNA-PKcs tilt. The N-HEAT 1–380, M-HEAT, FAT and kinase regions are colored as indicated. Cryo-EM map for putative DNA-PKcs-DNA-KU complex (Spagnolo et al., 2006) is shown in the bottom panel.
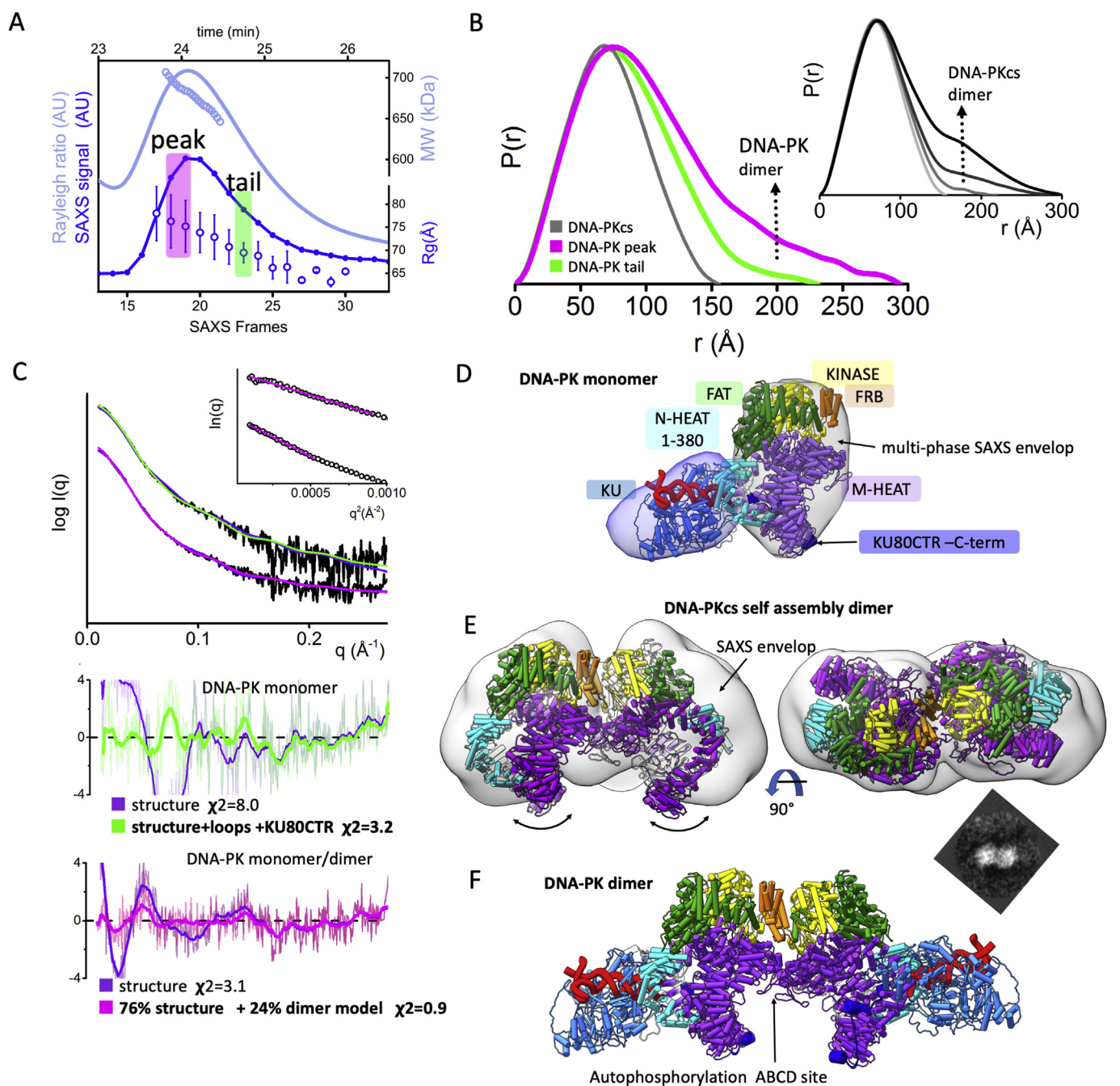
Fig. 4. Solution state of DNA-PK and its dimerization through the FRB domain.

A) SEC-MALS-SAXS chromatograms for DNA-PK assembly. Solid lines represent the MALS signal shown as Rayleigh signal (light blue) or integrated SAXS signal (dark blue) in arbitrary units, while symbols represent molecular weight (light blue) and R_g values for each collected SAXS frame (dark blue) versus elution time (taken from (Hammel et al., 2016).

B) Experimental (black) and theoretical (colored as indicated) SAXS profiles for the solution state of DNA-PK in monomeric and dimeric state. SAXS fits are shown together with the fit residuals and goodness of fit values (χ^2). Guinier plots for experimental SAXS curves are shown in inset.

C) Normalized pair distribution P(r) functions for experimental SAXS curves of DNA-PK assemblies measured at the peak and tail (green) of the elution peak (magenta) in comparison to monomeric DNA-PKcs taken from (Hammel et al., 2010a). Inset: Normalized P(r) functions calculate for the experimental SAXS curves of DNA-PKcs collected at protein concentrations 1.5, 3, 7 and 15 mg/ml (from light gray to black) indicates self-association of DNA-PKcs at higher concentrations (taken from (Hammel et al., 2010a)).

D) The cryo-EM structure of DNA-PK (Yin et al., 2017) is superimposed on to the multi-phase SAXS envelop of DNA-PK taken from (Hammel et al., 2016).

E) Two orthogonal views of DNA-PKcs docking model representing the self-association dimer. The DNA-PKcs self-association dimer superimposed on to the SAXS envelop reconstruction for the SAXS data collected at the 15 mg/ml protein concentration (taken from (Hammel et al., 2010a). Additional top scoring models are shown in the supplemental Fig. 2. The 2D EM projection of DNA-PKcs self-association dimer (taken from (Boskovic et al., 2003)).

F) Proposed atomic model of DNA-PK − dimer that was used in 24% weight to match the SAXS curve measured at the SEC elution peak (see panel A).

single state model showed a compact arrangement of KU80CTR neighboring the KU70 α/β domain (Fig. 1C). Significant improvement in the SAXS fit was achieved by selecting the multi-state model ($\chi^2_{single-state}$ 4.2 vs. $\chi^2_{two-state}$ 2.2, Fig. 1A). The multi-state model included 55% of the conformers with the KU80CTR domain in close proximity to the KU70 α/β domain and 45% of the conformers with detached KU80CTR, ~30 Å from the KU core (Fig. 1C). The larger weighting of compact structures in solution validates and extends the models observed in cryo-EM studies showing relatively compact low resolution molecular envelopes, which suggested close contacts between KU80CTR and KU70 α/β domains (Rivera-Calzada et al., 2007) (Fig. 1D). However, a significant population of detached KU80CTR may remain of mechanistic importance in recruiting of DNA-PKcs.

Next, SAXS analysis of the KU-DNA complex was prepared using 16bp double-stranded DNA with a short stem loop at one end as template (Hammel et al., 2010a). Similar to prior SAXS analysis of the KU-DNA complex (Hammel et al., 2010a), only small differences between KU and KU-DNA measurements were observed. Particularly, narrowing of the P(r) functions (Fig. 1B) indicates a less hollow structure that can be explained by insertion of DNA between the bridge and β barrel KU-regions (Walker et al., 2001). Again, conformational sampling was performed on KU80CTR to determine the movement of KU80CTR relative to the KU-DNA core. In the search for representative multi-state solution models, the KU-DNA experimental SAXS data was fit against a pool of ~10000 conformers including KU and KU-DNA models with various conformations of KU80CTR. Surprisingly, the best fit multi-state model showed only 18% of the KU-DNA complex with the KU80CTR in close proximity to the KU core (Fig. 1C). This partial occupancy of the KU-DNA complex suggests dissociation of KU from unprotected DNA. These results are in agreement with multiple assays under non-reducing condition (Andrews et al., 2006).

3.2. Conformational plasticity in the DNA-PKcs HEAT region

DNA-PKcs (4128 amino acids, ~469 kDa) (Hartley et al., 1995) is composed of FAT, Kinase, FAT-C domains that form the "head" or crown and a large, flexible HEAT region, also called the palm region, that can be divided into the M-HEAT (Williams et al., 2008; Rivera-Calzada et al., 2005; Sibanda et al., 2010) and the recently visualized N-terminal HEAT region (N-HEAT) (Sharif et al., 2017; Sibanda et al., 2017). DNA-PKcs structures, together with previously reported cryo-EM low-resolution molecular envelopes (Williams et al., 2008; Rivera-Calzada et al., 2005) suggest that the DNA-PKcs HEAT region is flexibly attached to the "head" region allowing it to move during autophosphorylation (Hammel et al., 2010a) and rearrange upon interaction with the KU-DNA complex (Yin et al., 2017). Our previous solution scattering studies have shown that DNA-PKcs undergoes self-association at higher protein concentrations (Hammel et al., 2010a). Dimer-free DNA-PKcs SAXS data revealed a typical globular particle with a D_{max} of 155 Å (Fig. 2B and Table 1).

To test how the existing atomic resolution structures match the solution state, we compared existing DNA-PKcs structures to experimental SAXS curves. The available atomic models are missing loop regions corresponding to amino acids 2576–2776 which contains the ABCDE cluster of phosphorylation sites (Douglas et al., 2002; Ding et al., 2003) located between the M-HEAT and FAT domain, and a conserved DNA-PK signature motif (Lees-Miller et al., 2020). Without these domains, fits of the X-ray crystal (Sibanda et al., 2017) and cryo-EM (Sharif et al., 2017; Yin et al., 2017) structures were poor ($\chi^2_{crystal}$ = 128 crystal and $\chi^2_{cryo-EM}$ = 160) (Fig. 2A). To further test whether this discrepancy was due to the flexibility of the missing regions, these sections were built using MODELLER (Sali and Blundell, 1993) and conformational sampling was applied using BILBOMD (Pelikan et al., 2009) to mimic the plasticity of the added regions. The goodness of SAXS fit improved by including flexibility in the ~2576–2776 region ($\chi^2_{single-state}$ = 25.3); however, the remaining discrepancy between theoretical and experimental SAXS curves in the low-resolution range (q 0.05-0.15 Å^{-1}, see Fig. 2A), suggested larger conformational rearrangements of the DNA-PKcs domains in solution.

To visualize these allosteric changes, the conformational sampling protocol was applied using normal mode analysis (NMA) (Panjkovich and Svergun, 2016). DNA-PKcs was divided into 4 regions (see Materials and methods) and constrained NMA sampling was applied to optimize the position of each region relative to the each other including normal mode movement inside each region. The best SAXS fit model was found by searching the two-state models (Schneidman-Duhovny et al., 2016) from the pool of existing structures and 10 models derived from NMA conformational sampling (NMA-model). The best two-state model included 38% of the original structure and 62% of the NMA-model, and was in excellent agreement with the experimental SAXS profile ($\chi^2_{two-state}$ = 5.8, Fig. 2A). The NMA-model showed a ~25 Å displacement of the N-HEAT domain (Fig. 2D) and agreed with the conformational variability of this region, as shown by comparison of the cryo-EM and crystal structures (Fig. 2C). Additionally, the NMA-model showed a smaller ~10 Å movement of the M-HEAT region. In sum, a multi-state model of DNA-PKcs was determined experimentally that shows the flexibility of the HEAT region in solution.

3.3. Displacement of the N-terminal HEAT domain during autophosphorylation suggests the release mechanism of DNA-PKcs from DNA-PK

Autophosphorylation of DNA-PKcs prompts its release from KU-DNA double strand break (DSB) complexes *in vitro* and in vivo (Hammel et al., 2010a; Douglas et al., 2007; Block et al., 2004; Uematsu et al., 2007; Jette and Lees-Miller, 2015). In prior studies, the *in vitro* autophosphorylated form of purified DNA-PKcs was isolated and analyzed using SAXS (Hammel et al., 2010a). Comparison of the SAXS data of DNA-PKcs with and without autophosphorylation revealed different scattering profiles over the entire observed scattering range (Fig. 2A). These changes were visualized in the P(r) function as broadening (Fig. 2B) and indicated a large conformational change involving the relocation of DNA-PKcs domains rather than extension of a single domain or a local change at the phosphorylation site. Calculated SAXS profiles from atomic resolution DNA-PKcs structures disagree with experimental SAXS profiles ($\chi^2_{cryo-EM}$ = 42.7). The large discrepancies seen between the theoretical and experimental profiles at low-resolution (q range 0.05–0.15 Å^{-1}, see Fig. 2A), further suggest a large conformational rearrangement.

Using a similar process to our analysis of non-phosphorylated DNA-PKcs, constrained NMA conformational sampling was performed to modify the position of the N-HEAT, M-HEAT, FAT, and Kinase regions (see Materials and methods). The best fit model was found by searching the two-state models from the pool of existing structures and multiple NMA derived models. The best two-state model, included 16% of conformations near the crystal structure (Sibanda et al., 2017) and 84% of the NMA-model. The two-state model fit was a great improvement over the single model fit and gave an excellent match to the experimental SAXS curve ($\chi^2_{two-state}$ = 5.8, Fig. 2A). The NMA-model showed large (~40 Å) displacements of both the N- and M-HEAT regions leading to closure of the aperture between these domains (Fig. 2D). Together with the extension of the M-HEAT region, the NMA-model explains the observed broadening of the P(r) function and the increasing R_g values relative to the non-phosphorylated DNA-PKcs. This atomistic model of autophosphorylated DNA-PKcs uncovers rearrangement

of the entire HEAT region suggesting inaccessibility of the KU/N-HEAT binding site (Yin et al., 2017). These results show that DNA-PKcs autophosphorylation conceals the interface between DNA-PKcs and KU. We hypothesize that by making the N-HEAT/KU binding site inaccessible, KU is forced to the detach from DNA-PKcs which subsequently allows other NHEJ processing enzymes, like DNA Ligase IV and polynucleotide kinase phosphatase (PNKP), to bind the DSB.

3.4. Two DNA-PKcs bridged by 40bp DNA form an "dumbbell" arrangement

Previously we showed similarity between the low resolution (33 Å) DNA-PK cryo-EM map (EMD1210), (Spagnolo et al., 2006) and SAXS envelopes of the dumbbell arrangement of two DNA-PKcs molecules bridged by a 40-bp duplex with a Y-shaped structure at one end (40bp Y-DNA) (Hammel et al., 2010a) (Fig. 3). We also found that a more compact dumbbell dimer is formed in the presence of 40bp DNA with the hairpin (40bp H-DNA) and 40bp DNA with two blunt ends (40bp DNA) (Hammel et al., 2010a). Distinct dumbbell arrangements in the presence of 40bpY-DNA were interpreted as a bridging of two DNA-PKcs with the bulky head regions pointing outward, whereas the more compact DNA-PKcs - 40bp H-DNA and DNA-PKcs - 40bp DNA dimers were explained by a head to head arrangement.

Here we used SAXS with atomistic models to test formation of the dumbbell arrangement and consider the capability of DNA-PKcs to bind various DNA ends in the absence of KU. The DNA-binding site within the N-HEAT and M-HEAT aperture is rich in positively-charged residues mostly located on the N-HEAT 1−380 region (Yin et al., 2017). The lack of specific protein-DNA contacts and the opened DNA-binding site may allow DNA-PKcs to accommodate a wide spectrum of DNA ends (Yin et al., 2017). Disappearance of the dimeric state in the excess of DNA (Fig. 3A) (Hammel et al., 2010a) further supports the notion that the DNA-PKcs-DNA interaction is not stably maintained without KU (Yin et al., 2017; Yoo and Dynan, 1999). By preserving the DNA binding site and mimicking conformational variability of the N-HEAT 1−380 region, DNA-PKcs can adopt different tilts relative to the linear DNA (Fig. 3C). To fit the SAXS data, we used a pool of dimer models build based on DNA-PK structure (Yin et al., 2017) (see Methods). The best fit for the DNA-PKcs-40bp DNA dimer was obtained by a two-state model that includes 56% of the dimer using DNA-PKcs crystal structure (model 1) (Sibanda et al., 2017) and 44% of the dimer using DNA-PKcs taken from the DNA-PK structure (model 2) (Yin et al., 2017). This two-state model gives a significant improvement in the SAXS fit over the single model ($\chi2_{single-state} = 5.0$ vs. $\chi2_{two-state} = 1.8$, Fig. 3B). Model 1 and model 2 (65% and 35%) were also selected to give best SAXS fit of DNA-PKcs - 40bp H-DNA data with the significant improvement over the single model fit ($\chi2_{single-state} = 3.8$ vs. $\chi2_{two-state} = 1.3$, Fig. 3B). On the other hand, the extended dimer of DNA-PKcs − 40bp Y-DNA was well matched with extended single model 1, whereas only a non-significant improvement in the SAXS fit was obtained by two-state model ($\chi2_{single-state} = 5.0$ vs. $\chi2_{two-state} = 5.3$, Fig. 3B). These observations suggest a dominant presence of the extended dumbbell assembly: they further agree with well separated peaks in P(r) function (Fig. 3A) and distinct volumes in the SAXS envelope (Fig. 3C). Yet, this ability of DNA-PKcs to assemble on both ends of the DNA structure as visualized here and in previous studies (Spagnolo et al., 2006) may not be physiologically relevant, as in vivo DNA damage-induced DSBs would each have only one exposed DNA end. In contrast, the self-association in the DNA-PKcs dimer, provides an appropriate protein arrangement for the initial NHEJ step and is further described in the next section.

3.5. DNA-PK dimer reconstruction

In prior work (Hammel et al., 2016), the overall DNA-PK complex architecture was characterized in solution with KU bound to a short dsDNA oligomer mimicking a DSB. For the current experiments, DNA-PKcs was mixed with KU that had been pre-incubated with 20 bp DNA duplex containing a short DNA stem-loop on one end and a 5′-nucleotide overhang on the other. SEC-SAXS-MALS measurements, complimented by SDS-PAGE analysis of the SEC fractions, confirmed the DNA-PK assembly. DNA-PK eluted as an asymmetric peak (Fig. 3A), whereas MALS-analysis showed a decrease in the molecular weight (MW) of DNA-PK from 750 kDa at the beginning of elution peak to ~650 kDa at the tail (Fig. 4A). Thus, under these experimental conditions, we found that DNA-PK was primarily forming a 1:1:1 assembly with a theoretical MW of 642 kDa. Analysis of SAXS frames across the primary elution peak also showed a decrease in R_g from ~75 Å at the peak to ~65 Å at the tail (Fig. 4A, Table 1). These SEC-SAXS-MALS results suggest formation of a transient DNA-PK dimer that slowly interconverts over the elution time into a DNA-PK 1:1:1 assembly (DNA-PKcs:KU:DNA). The formation of a DNA-PK dimer agrees with the tendency of DNA-PKcs to self-associate (Hammel et al., 2010a; Boskovic et al., 2003) (Fig. 4C inset).

To further analyze both monomeric and dimeric solution states of DNA-PK, the primary SEC elution peak was deconvoluted into two SAXS profiles (peak and tail, Fig. 4B). The P(r) function calculated for the SAXS curve at the elution peak showed an elongated assembly with a D_{max} of ~300 Å, while the P(r) from the tail was narrower with a D_{max} of ~220 Å (Fig. 4C). Due to the expected transient dimerization of DNA-PK, the SAXS curves collected at the peak and tail of the SEC were fit separately.

The monomeric DNA-PK model built based on a cryo-EM structure (Yin et al., 2017) matched well to the SAXS profile from the elution tail (Fig. 4B). However, adding the missing parts of DNA-PKcs and KU, including the KU80CTR domain to the model improved the fit ($\chi2_{structure} = 8.0$ vs. $\chi2_{full\ model} = 3.6$) (Fig. 4B). Further refinement of KU80CTR location relative to the KU core was not possible due to low signal-to-noise in the SAXS data. Nevertheless, the overall arrangement of DNA-PK supported and extended reported multi-phase SAXS envelops (Hammel et al., 2016) and further confirmed the overall DNA-PK architecture in solution (Fig. 4D).

To build the DNA-PK dimer model, we initially modeled the DNA-PKcs dimer through the molecular docking of two DNA-PKcs monomers using a rigid docking, geometric shape-matching algorithm (Schneidman-Duhovny et al., 2005). The best scoring model showed two DNA-PKcs monomers (Sibanda et al., 2017) in a mirror symmetry with a head-to-head arrangement (Fig. 4E). Overall, the observed arrangement of self-associated DNA-PKcs resembled the previously reported V-like SAXS envelop (Hammel et al., 2010a) and low resolution 2D EM projection (Boskovic et al., 2003) (Fig. 4E−inset). Furthermore, the docking model suggested contact between FKBP12-rapamycin-binding domains (FRB) which are conserved within the PI3K kinase family members (Fig. 4E). While the role of the FRB domain is unclear, there is evidence from mTOR studies that it might act as a gatekeeper that restricts access to the catalytic site (Yang et al., 2017). The stand-alone FRB domain appears to function as gate to the buried and conserved T3950 autophosphorylation site (Sibanda et al., 2017) that deactivates the kinase (Douglas et al., 2007). The dimerization interface of DNA-PKcs modeled in this study may alter FRB positioning and control access to the T3950 autophosphorylation site.

Building upon these results, atomic models of the DNA-PK dimer were constructed by aligning two DNA-PK monomers with the DNA-PKcs dimer. Exchange between the two states occurred over the course of purification, so that a pure dimeric state could not be
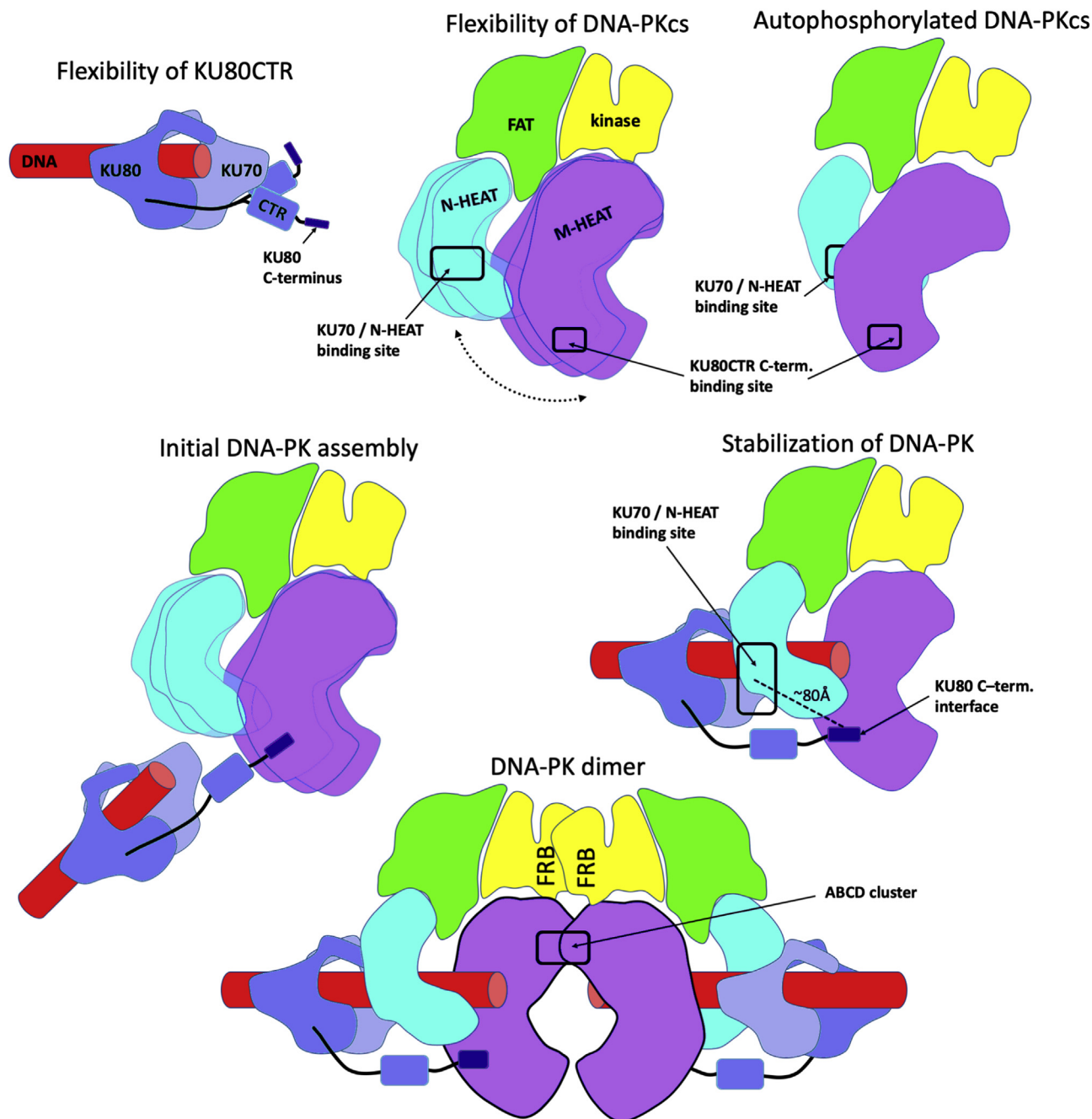
Fig. 5. DNA-PK functional flexibility as cartoons. i) Minimal flexibility of KU80CTR and extension of its C-terminus. ii) Flexibility of HEAT domain relatively to the DNA-PKcs head region. iii) N and M-HEAT rearrangement upon the DNA-PKcs autophosphorylation. iv) Extension of the KU80 "arm" during initial DNA-PK assembly. v) Stabilization of the DNA-PK assembly by multiple protein-protein and protein-DNA interactions. vi) Proposed DNA-PK dimer arrangement.

isolated from the monomeric one. Thus, the SAXS curve generated from the SEC peak was fit against a library of atomic models including DNA-PKcs structures, DNA-PKcs models, DNA-PK monomer, and DNA-PK dimer. The best fit two-state model was obtained by including 24% of DNA-PK dimer and 76% of DNA-PK monomer conferring an excellent match to the experimental SAXS profile ($\chi2 = 0.9$, Fig. 4BE). The SAXS modeling together with the determined MW demonstrated the tendency of DNA-PK to form a head-to-head dimer with a V-shape arrangement. In the model, KU-DNA was positioned at the extremity of the dimer with the DNA entering an aperture in DNA-PKcs between the N- and M-HEAT regions.

4. Discussion

The promise of macromolecular structural biology is to visualize structures that unveil critical functional mechanisms. This promise is too often not fully realized due to missing or incomplete knowledge of functional conformations assessed outside of cryo- and solid-state conditions (Putnam et al., 2007). On the other hand, SAXS, which can be high-throughput and directly measures thermodynamic solution-state conformational states and assemblies, is resolution limited. Yet, SAXS can be combined with other measurements to interrogate atomic level information Rambo and Tainer, 2013b. Here we assess practical and robust methods to join

SAXS with cryo-EM and X-ray crystallographic data as applied to the dynamic structure of DNA-PKcs and its interactions with KU and DNA in solution. The results reported provide insights into the dynamic architectural changes whereby these complexes orchestrate non-sequential NHEJ repair (Yano and Chen, 2008; Cottarel et al., 2013; Wang and Lees-Miller, 2013). Previously our SAXS results predicted XRCC4 and XLF protein filaments for DNA end protection and alignment in DSBR (Hammel et al., 2010b, 2011), and these filaments were subsequently identified in single-molecule experiments as well as in cells (Wang et al., 2018; Reid et al., 2015). Importantly, the new results presented here uncover displacement of the N-terminal HEAT domain during autophosphorylation as suitable for a regulated release mechanism of DNA-PKcs from DNA-PK to control unproductive access to toxic and mutagenic DNA repair intermediates. Such release of unproductive complexes has been seen before for FEN1 and XPG nuclease functions in base and nucleotide excision repair (Tsutakawa et al., 2017, 2020; Rashid et al., 2017). Overall, we present new SAXS data, revisit solution structure modeling of the KU heterodimer, and combine SAXS measurements with atomic resolution static structures.

Our improved experiments on KU reveal that a major population of KU80CTR is mostly located in close proximity to the KU core. However, a nearly equal part (45%) of the solution state involves an extension of KU80CTR domain through the flexible linker (Fig. 1C) that is in apparent disagreement with the static picture of KU visualized by cryo-EM (Rivera-Calzada et al., 2007). Yet, our results support and extend earlier studies showing proteolytic sensitivity of the KU80CTR (Paillard and Strauss, 1993; Mo and Dynan, 2002) and subsequent structural studies revealing a disordered linker region (Harris et al., 2004). We reason that the detachment of KU80CTR from KU core remains functionally important for its role in the recruiting of DNA-PKcs. By superimposing DNA-PK and DNA-PKcs-KU80CTR structures (Sibanda et al., 2017; Yin et al., 2017), we can determine the distance between the KU core and KU80CTR (Fig. 4D). When KU is bound to DNA-PKcs, the KU80CTR region needs to be far more extended from the KU core (~60 Å) than in the free state (Fig. 5). Additionally, the C-terminal interaction motif of KU80CTR (Gell and Jackson, 1999), which is predicted to have helical propensity, is even more distant (~80 Å) from the KU core (Sibanda et al., 2017). Thus, the KU80CTR domain including the KU80CTR C-terminus needs to undergo a large displacement during KU interaction with DNA-PKcs. Such a dramatic rearrangement is enabled by the length of the KU80CTR linker (~60 residues). To initiate complexation, the flexibly tethered KU80CTR C-terminus helix needs to find the binding site near the "PQR" autophosphorylation cluster (Sibanda et al., 2017; Chen et al., 2005). This initial KU-tethering is followed by recruitment of the KU core to the N-HEAT binding site, allowing insertion of the DNA end into the M-/N-HEAT aperture (Fig. 5). The relatively compact arrangement of KU80CTR in the absence and presence of DNA suggests that this KU80CTR rearrangement is initiated by interaction between the KU80CTR C-terminus and the M-HEAT domain (Sibanda et al., 2017) rather than by DNA binding (Fig. 5).

Alone, DNA-PKcs interacts with DNA with low affinities (Yoo and Dynan, 1999). However, its ability to assemble on various ends of the DNA structure can lead to formation of dumbbell arrangement with two DNA-PKcs binding DNA ends (Hammel et al., 2010a). This DNA-PKcs dimer arrangement is evidently not physiologically relevant, because in vivo DNA damage induced DSBs would each have only one exposed DNA end. A tighter interaction between DNA-PKcs and DNA is supported by KU (Fig. 5) (Yin et al., 2017; Hammel et al., 2010a; Jette and Lees-Miller, 2015). DNA-PKcs and KU together form a DNA-binding tunnel where DNA duplex fills the aperture between the N-HEAT and the M-HEAT region of DNA-PKcs (Yin et al., 2017). We find that in solution the N-HEAT region

undergoes large motions in free DNA-PKcs (Fig. 5), in agreement with the conformational variability between reported DNA-PKcs structures (Sharif et al., 2017; Baretic et al., 2019; Sibanda et al., 2017) (Fig. 2C), as well between two DNA-PKcs chains from the crystal structure (Sibanda et al., 2017). Larger movement of N-HEAT and M-HEAT regions in solution (Fig. 2D) correlate with much smaller changes in conformation and position of the HEAT regions observed in the crystal and cryo-EM structure. In the DNA-PK structure (Yin et al., 2017) the N-HEAT domain is displaced by ~35 Å inwards towards the FAT domain upon binding with KU-DNA (Fig. 2C). Our solution-based modeling shows similar movement of the N-HEAT domain in the absence of KU-DNA (Fig. 2D), which supports the importance of inherent flexibility in this domain upon DNA-PK activation. Conformational adaptability of the N-HEAT region, bending of KU70 (Yin et al., 2017), and bridging of the KU80CTR C-terminus with the M-HEAT domain all contribute to a lock-in mechanism that stabilizes the formation of the DNA-PK assembly (Fig. 5). Such a mechanism would ensure that assembly of DNA-PK controls a molecular switch needed to transfer the activation signal from the KU80CTR binding site to the kinase located in the head region ~100 Å away (Fig. 5).

Formation of a small but significant population of dimeric DNA-PK in solution (Fig. 4B) suggests that self-association of DNA-PKcs (Hammel et al., 2010a) (Fig. 4E) may support the dimerization of the DNA-PK complex. Here modeled head-to-head arrangement of the DNA-PKcs dimer resembles the arrangement of the closely related ATM kinase dimer (Baretic et al., 2017). This arrangement raises the question of whether the FRB dimerization controls the autophosphorylation, which activates the release of DNA-PKcs from the NHEJ presynaptic complex (Ding et al., 2003; Block et al., 2004; Cui et al., 2005).

The main rearrangement of DNA-PKcs during autophosphorylation shows widening of the M-HEAT region (Fig. 2D) that allows the N-terminal domain (1—370) of the N-HEAT to slide in to the cradle formed by wider M-HEAT region (Fig. 5). We hypothesize that this mechanism may conceal the binding site for KU70 (Fig. 5) and trigger release of DNA-PKcs from the DNA ends.

Autophosphorylation-induced domain rearrangement furthermore has the potential to affect the interaction of DNA-PKcs with accessory proteins, which may further regulate NHEJ in vivo. These collective results and ideas support and extend our previous structural understanding of DNA-PK activation and flexibility. Specifically, integrating SAXS measurements with the atomistic modeling utilizing crystal and cryo-EM structures provides data-based dynamic models that suggest how KU and DNA-PKcs combine and assemble enzymatically to promote structural and catalytic activities for NHEJ initiation and the choreography of DSB repair. Going forward will be interesting to see how RNA may regulate or active these DNA-PK complexes (Lees-Miller et al., 2016). Furthermore, in this and other efforts to combine advanced cryo-EM with SAXS, the use of gold-label SAXS may provide a means to reduce SAXS samples needs substantially (Hura et al., 2013b).

5. Synopsis and perspective

NHEJ mechanisms must be fast, flexible and accurate while accommodating alignment components and active ligase conformations along with two DNA ends. These features cannot be conveyed by a single structure. However single structures do provide a starting point for analyzing solution based information that typically contains averaged or single distance information like FRET or SAXS. Here we describe our analysis of SAXS data on the central DNA-PK assembly and its components DNA-PKcs, and KU in the context of new cryo-EM and crystallographic structures. While the static cryo-EM or crystallographic structures alone cannot decipher

functional dynamicity at the observed atomic resolution, by adding a solution-based atomistic modeling we are able to visualize conformational switches likely to be required for assembly and disassembly of DNA-PK complex. In general, these combined SAXS and atomic structural analyses on this biologically and medically important and exemplary DNA repair complex provide and test an enabling approach for robust data-based models of functional mechanisms in dynamic macromolecular complexes with relevance to cancer biology and therapeutics.

Acknowledgements

Appendix A. Supplementary data

Supplementary data to this article can be found online at https://doi.org/10.1016/j.pbiomolbio.2020.09.003.

Abbreviations

ATM	ataxia telangiectasia mutated;
cryo-EM	cryo-electron microscopy;
ds	double-stranded;
DSB	DNA double strand break;
DSBR	DNA double strand break repair;
DNA-PK	DNA-activated/dependent protein kinase;
DNA-PKcs	DNA-PK catalytic subunit;
FAT	FRAP, ATM and TRRAP;
FRB	FKBP12-rapamycin-binding domains;
HEAT	Huntingtin, Elongation factor, PP2A-A subunit, TOR;
KU	KU70/KU80 heterodimer;
KU80CTR	KU80 C-terminal region;
MX	macromolecular X-ray crystallography;
NHEJ	non-homologous end joining;
N-HEAT	N-terminal HEAT domain;
M-HEAT	central HEAT domain;
NMA	normal mode analysis;
MALS	multi-angle light scattering;
PI3K	phosphatidyl inositol 3 kinase;
SAP	SAF-A/B, Acinus and PIAS;
SAXS	small-angle X-ray scattering;
SEC	size exclusion chromatography;
SEC-SAXS-MALS	size exclusion chromatography coupled with in-line SAXS and multi-angle light scattering;

References

Andrews, B.J., Lehman, J.A., Turchi, J.J., 2006. Kinetic analysis of the Ku-DNA binding activity reveals a redox-dependent alteration in protein structure that stimulates dissociation of the Ku-DNA complex. J. Biol. Chem. 281, 13596—13603.

Bacolla, A., Tainer, J.A., Vasquez, K.M., Cooper, D.N., 2016. Translocation and deletion breakpoints in cancer genomes are associated with potential non-B DNA-forming sequences. Nucleic Acids Res. 44, 5673—5688.

Baretic, D., Pollard, H.K., Fisher, D.I., Johnson, C.M., Santhanam, B., Truman, C.M., et al., 2017. Structures of closed and open conformations of dimeric human ATM. Sci. Adv. 3, e1700933.

Baretic, D., Maia de Oliveira, T., Niess, M., Wan, P., Pollard, H., Johnson, C.M., et al., 2019. Structural insights into the critical DNA damage sensors DNA-PKcs, ATM and ATR. Prog. Biophys. Mol. Biol. 147, 4—16.

Block, W.D., Yu, Y., Merkle, D., Gifford, J.L., Ding, Q., Meek, K., et al., 2004. Autophosphorylation-dependent remodeling of the DNA-dependent protein kinase catalytic subunit regulates ligation of DNA ends. Nucleic Acids Res. 32, 4351—4357.

Boskovic, J., Rivera-Calzada, A., Maman, J.D., Chacon, P., Willison, K.R., Pearl, L.H., et al., 2003. Visualization of DNA-induced conformational changes in the DNA repair kinase DNA-PKcs. EMBO J. 22, 5875—5882.

Brosey, C.A., Tainer, J.A., 2019. Evolving SAXS versatility: solution X-ray scattering for macromolecular architecture, functional landscapes, and integrative structural biology. Curr. Opin. Struct. Biol. 58, 197—213.

Bryant, H.E., Schultz, N., Thomas, H.D., Parker, K.M., Flower, D., Lopez, E., et al., 2005. Specific killing of BRCA2-deficient tumours with inhibitors of poly(ADP-ribose) polymerase. Nature 434, 913—917.

Chan, D.W., Mody, C.H., Ting, N.S., Lees-Miller, S.P., 1996. Purification and characterization of the double-stranded DNA-activated protein kinase, DNA-PK, from human placenta. Biochem. Cell. Biol. 74, 67—73.

Chen, B.P., Chan, D.W., Kobayashi, J., Burma, S., Asaithamby, A., Morotomi-Yano, K., et al., 2005. Cell cycle dependence of DNA-dependent protein kinase phosphorylation in response to DNA double strand breaks. J. Biol. Chem. 280, 14709—14715.

Classen, S., Hura, G.L., Holton, J.M., Rambo, R.P., Rodic, I., McGuire, P.J., et al., 2013. Implementation and performance of SIBYLS: a dual endstation small-angle X-ray scattering and macromolecular crystallography beamline at the Advanced Light Source. J. Appl. Crystallogr. 46, 1—13.

Cottarel, J., Frit, P., Bombarde, O., Salles, B., Negrel, A., Bernard, S., et al., 2013. A noncatalytic function of the ligation complex during nonhomologous end joining. J. Cell Biol. 200, 173—186.

Cui, X., Yu, Y., Gupta, S., Cho, Y.M., Lees-Miller, S.P., Meek, K., 2005. Autophosphorylation of DNA-dependent protein kinase regulates DNA end processing and may also alter double-strand break repair pathway choice. Mol. Cell. Biol. 25, 10842—10852.

Ding, Q., Reddy, Y.V., Wang, W., Woods, T., Douglas, P., Ramsden, D.A., et al., 2003. Autophosphorylation of the catalytic subunit of the DNA-dependent protein kinase Is required for efficient end processing during DNA double-strand break repair. Mol. Cell. Biol. 23, 5836—5848.

Douglas, P., Sapkota, G.P., Morrice, N., Yu, Y., Goodarzi, A.A., Merkle, D., et al., 2002. Identification of in vitro and in vivo phosphorylation sites in the catalytic subunit of the DNA-dependent protein kinase. Biochem. J. 368, 243—251.

Douglas, P., Cui, X., Block, W.D., Yu, Y., Gupta, S., Ding, Q., et al., 2007. The DNA-dependent protein kinase catalytic subunit is phosphorylated in vivo on threonine 3950, a highly conserved amino acid in the protein kinase domain. Mol. Cell. Biol. 27, 1581—1591.

Dutta, A., Eckelmann, B., Adhikari, S., Ahmed, K.M., Sengupta, S., Pandey, A., et al., 2017. Microhomology-mediated end joining is activated in irradiated human cells due to phosphorylation-dependent formation of the XRCC1 repair complex. Nucleic Acids Res. 45, 2585—2599.

Dyer, K.N., Hammel, M., Rambo, R.P., Tsutakawa, S.E., Rodic, I., Classen, S., et al., 2014. High-throughput SAXS for the characterization of biomolecules in solution: a practical approach. Methods Mol. Biol. 1091, 245—258.

Eckelmann, B.J., Bacolla, A., Wang, H., Ye, Z., Guerrero, E.N., Jiang, W., et al., 2020. XRCC1 promotes replication restart, nascent fork degradation and mutagenic DNA repair in BRCA2-deficient cells. NAR Canc. 2, zcaa013.

Gell, D., Jackson, S.P., 1999. Mapping of protein-protein interactions within the DNA-dependent protein kinase complex. Nucleic Acids Res. 27, 3494—3502.

Ghezraoui, H., Piganeau, M., Renouf, B., Renaud, J.B., Sallmyr, A., Ruis, B., et al., 2014. Chromosomal translocations in human cells are generated by canonical nonhomologous end-joining. Mol. Cell 55, 829—842.

Goodarzi, A.A., Lees-Miller, S.P., 2004. Biochemical characterization of the ataxia-telangiectasia mutated (ATM) protein from human cells. DNA Repair (Amst) 3, 753—767.

Hammel, M., 2012. Validation of macromolecular flexibility in solution by small-angle X-ray scattering (SAXS). Eur. Biophys. J. 41, 789—799.

Hammel, M., Yu, Y., Mahaney, B.L., Cai, B., Ye, R., Phipps, B.M., et al., 2010a. Ku and DNA-dependent protein kinase dynamic conformations and assembly regulate DNA binding and the initial non-homologous end joining complex. J. Biol. Chem. 285, 1414—1423.

Hammel, M., Yu, Y., Fang, S., Lees-Miller, S.P., Tainer, J.A., 2010b. XLF regulates filament architecture of the XRCC4.ligase IV complex. Structure 18, 1431—1442.

Hammel, M., Rey, M., Yu, Y., Mani, R.S., Classen, S., Liu, M., et al., 2011. XRCC4 protein interactions with XRCC4-like factor (XLF) create an extended grooved scaffold for DNA ligation and double strand break repair. J. Biol. Chem. 286, 32638—32650.

Hammel, M., Yu, Y., Radhakrishnan, S.K., Chokshi, C., Tsai, M.S., Matsumoto, Y., et al., 2016. An intrinsically disordered APLF links Ku, DNA-PKcs and XRCC4-DNA ligase IV in an extended flexible non-homologous end joining complex. J. Biol. Chem. 291, 26987—27006.

Harris, R., Esposito, D., Sankar, A., Maman, J.D., Hinks, J.A., Pearl, L.H., et al., 2004. The 3D solution structure of the C-terminal region of Ku86 (Ku86CTR). J. Mol. Biol. 335, 573—582.

Hartley, K.O., Gell, D., Smith, G.C., Zhang, H., Divecha, N., Connelly, M.A., et al., 1995. DNA-dependent protein kinase catalytic subunit: a relative of phosphatidylinositol 3-kinase and the ataxia telangiectasia gene product. Cell 82, 849—856.

Horst, B.G., Yokom, A.L., Rosenberg, D.J., Morris, K.L., Hammel, M., Hurley, J.H., et al., 2019. Allosteric activation of the nitric oxide receptor soluble guanylate cyclase mapped by cryo-electron microscopy. eLife 8.

Houl, J.H., Ye, Z., Brosey, C.A., Balapiti-Modarage, L.P.F., Namjoshi, S., Bacolla, A., et al., 2019. Selective small molecule PARG inhibitor causes replication fork stalling and cancer cell death. Nat. Commun. 10, 5654.

Hura, G.L., Budworth, H., Dyer, K.N., Rambo, R.P., Hammel, M., McMurray, C.T., et al., 2013. Comprehensive macromolecular conformations mapped by quantitative SAXS analyses. Nat. Methods 10, 453–454.

Hura, G.L., Menon, A.L., Hammel, M., Rambo, R.P., Poole 2nd, F.L., Tsutakawa, S.E., et al., 2009. Robust, high-throughput solution structural analyses by small angle X-ray scattering (SAXS). Nat. Methods 6, 606–612.

Hura, G.L., Tsai, C.L., Claridge, S.A., Mendillo, M.L., Smith, J.M., Williams, G.J., et al., 2013b. DNA conformations in mismatch repair probed in solution by X-ray scattering from gold nanocrystals. Proc. Natl. Acad. Sci. U. S. A. 110, 17308–17313.

Jette, N., Lees-Miller, S.P., 2015. Prog Biophys Mol Biol. 117 (2-3), 194–205. https://doi.org/10.1016/j.pbiomolbio.2014.12.003. Epub 2014 Dec 27.PMID: 25550082.

Kashammer, L., Saathoff, J.H., Lammens, K., Gut, F., Bartho, J., Alt, A., et al., 2019. Mechanism of DNA end sensing and processing by the Mre11-Rad50 complex. Mol. Cell 76, 382–394 e6.

Knott, G.J., Cress, B.F., Liu, J.J., Thornton, B.W., Lew, R.J., Al-Shayeb, B., et al., 2019. Structural basis for AcrVA4 inhibition of specific CRISPR-Cas12a. eLife 8.

Lafrance-Vanasse, J., Williams, G.J., Tainer, J.A., 2015. Envisioning the dynamics and flexibility of Mre11-Rad50-Nbs1 complex to decipher its roles in DNA replication and repair. Prog. Biophys. Mol. Biol. 117, 182–193.

Lees-Miller, S.P., Beattie, T.L., Tainer, J.A., 2016. Noncoding RNA joins Ku and DNA-PKcs for DNA-break resistance in breast cancer. Nat. Struct. Mol. Biol. 23, 509–510.

Lees-Miller, J.P., Cobban, A., Katsonis, P., Bacolla, A., Tsutakawa, S.E., Hammel, M., et al., 2020. Uncovering DNA-PKcs ancient phylogeny, unique sequence motifs and insights for human disease. Prog. Biophys. Mol. Biol. (this issue).

Mo, X., Dynan, W.S., 2002. Subnuclear localization of Ku protein: functional association with RNA polymerase II elongation sites. Mol. Cell. Biol. 22, 8088–8099.

Paillard, S., Strauss, F., 1993. Site-specific proteolytic cleavage of Ku protein bound to DNA. Proteins 15, 330–337.

Panjkovich, A., Svergun, D.I., 2016. Deciphering conformational transitions of proteins by small angle X-ray scattering and normal mode analysis. Phys. Chem. Chem. Phys. 18, 5707–5719.

Pelikan, M., Hura, G.L., Hammel, M., 2009. Structure and flexibility within proteins as identified through small angle X-ray scattering. Gen. Physiol. Biophys. 28, 174–189.

Putnam, C.D., Hammel, M., Hura, G.L., Tainer, J.A., 2007. X-ray solution scattering (SAXS) combined with crystallography and computation: defining accurate macromolecular structures, conformations and assemblies in solution. Q. Rev. Biophys. 40, 191–285.

Radhakrishnan, S.K., Lees-Miller, S.P., 2017. DNA requirements for interaction of the C-terminal region of Ku80 with the DNA-dependent protein kinase catalytic subunit (DNA-PKcs). DNA Repair 57, 17–28.

Rambo, R.P., Tainer, J.A., 2011. Characterizing flexible and intrinsically unstructured biological macromolecules by SAS using the Porod-Debye law. Biopolymers 95, 559–571.

Rambo, R.P., Tainer, J.A., 2013a. Accurate assessment of mass, models and resolution by small-angle scattering. Nature 496, 477–481.

Rambo, R.P., Tainer, J.A., 2013b. Super-resolution in solution X-ray scattering and its applications to structural systems biology. Annu. Rev. Biophys. 42, 415–441.

Rashid, F., Harris, P.D., Zaher, M.S., Sobhy, M.A., Joudeh, L.I., Yan, C., et al., 2017. Single-molecule FRET unveils induced-fit mechanism for substrate selectivity in flap endonuclease 1. eLife 6.

Reid, D.A., Keegan, S., Leo-Macias, A., Watanabe, G., Strande, N.T., Chang, H.H., et al., 2015. Organization and dynamics of the nonhomologous end-joining machinery during DNA double-strand break repair. Proc. Natl. Acad. Sci. U. S. A. 112, E2575–E2584.

Rivera-Calzada, A., Maman, J.D., Spagnolo, L., Pearl, L.H., Llorca, O., 2005. Three-dimensional structure and regulation of the DNA-dependent protein kinase catalytic subunit (DNA-PKcs). Structure 13, 243–255.

Rivera-Calzada, A., Spagnolo, L., Pearl, L.H., Llorca, O., 2007. Structural model of full-length human Ku70-Ku80 heterodimer and its recognition of DNA and DNA-PKcs. EMBO Rep. 8, 56–62.

Sali, A., Blundell, T.L., 1993. Comparative protein modelling by satisfaction of spatial restraints. J. Mol. Biol. 234, 779–815.

Schneidman-Duhovny, D., Hammel, M., 2018. Modeling structure and dynamics of protein complexes with SAXS profiles. Methods Mol. Biol. 1764, 449–473.

Schneidman-Duhovny, D., Inbar, Y., Nussinov, R., Wolfson, H.J., 2005. PatchDock and SymmDock: servers for rigid and symmetric docking. Nucleic Acids Res. 33, W363–W367.

Schneidman-Duhovny, D., Hammel, M., Sali, A., 2010. FoXS: a web server for rapid computation and fitting of SAXS profiles. Nucleic Acids Res. 38, W540–W544.

Schneidman-Duhovny, D., Hammel, M., Tainer, J.A., Sali, A., 2013. Accurate SAXS profile computation and its assessment by contrast variation experiments. Biophys. J. 105, 962–974.

Schneidman-Duhovny, D., Hammel, M., Tainer, J.A., Sali, A., FoXS, FoXSDock, MultiFoXS, 2016. Single-state and multi-state structural modeling of proteins and their complexes based on SAXS profiles. Nucleic Acids Res. 44, W424–W429.

Sharif, H., Li, Y., Dong, Y., Dong, L., Wang, W.L., Mao, Y., et al., 2017. Cryo-EM structure of the DNA-PK holoenzyme. Proc. Natl. Acad. Sci. U. S. A. 114, 7367–7372.

Shibata, A., Moiani, D., Arvai, A.S., Perry, J., Harding, S.M., Genois, M.M., et al., 2014. DNA double-strand break repair pathway choice is directed by distinct MRE11 nuclease activities. Mol. Cell 53, 7–18.

Sibanda, B.L., Chirgadze, D.Y., Blundell, T.L., 2010. Crystal structure of DNA-PKcs reveals a large open-ring cradle comprised of HEAT repeats. Nature 463, 118–121.

Sibanda, B.L., Chirgadze, D.Y., Ascher, D.B., Blundell, T.L., 2017. DNA-PKcs structure suggests an allosteric mechanism modulating DNA double-strand break repair. Science 355, 520–524.

Spagnolo, L., Rivera-Calzada, A., Pearl, L.H., Llorca, O., 2006. Three-dimensional structure of the human DNA-PKcs/Ku70/Ku80 complex assembled on DNA and its implications for DNA DSB repair. Mol. Cell 22, 511–519.

Spagnolo, L., Barbeau, J., Curtin, N.J., Morris, E.P., Pearl, L.H., 2012. Visualization of a DNA-PK/PARP1 complex. Nucleic Acids Res. 40, 4168–4177.

Syed, A., Tainer, J.A., 2018. The MRE11-RAD50-NBS1 complex conducts the orchestration of damage signaling and outcomes to stress in DNA replication and repair. Annu. Rev. Biochem. 87, 263–294.

Tsutakawa, S.E., Thompson, M.J., Arvai, A.S., Neil, A.J., Shaw, S.J., Algasaier, S.I., et al., 2017. Phosphate steering by Flap Endonuclease 1 promotes 5'-flap specificity and incision to prevent genome instability. Nat. Commun. 8, 15855.

Tsutakawa, S.E., Sarker, A.H., Ng, C., Arvai, A.S., Shin, D.S., Shih, B., et al., 2020. Human XPG nuclease structure, assembly, and activities with insights for neurodegeneration and cancer from pathogenic mutations. Proc. Natl. Acad. Sci. U. S. A. 117, 14127–14138.

Uematsu, N., Weterings, E., Yano, K., Morotomi-Yano, K., Jakob, B., Taucher-Scholz, G., et al., 2007. Autophosphorylation of DNA-PKCS regulates its dynamics at DNA double-strand breaks. J. Cell Biol. 177, 219–229.

Walker, J.R., Corpina, R.A., Goldberg, J., 2001. Structure of the Ku heterodimer bound to DNA and its implications for double-strand break repair. Nature 412, 607–614.

Wang, C., Lees-Miller, S.P., 2013. Detection and repair of ionizing radiation-induced DNA double strand breaks: new developments in nonhomologous end joining. Int. J. Radiat. Oncol. Biol. Phys. 86, 440–449.

Wang, J.L., Duboc, C., Wu, Q., Ochi, T., Liang, S., Tsutakawa, S.E., et al., 2018. Dissection of DNA double-strand-break repair using novel single-molecule forceps. Nat. Struct. Mol. Biol. 25, 482–487.

Williams, D.R., Lee, K.J., Shi, J., Chen, D.J., Stewart, P.L., 2008. Cryo-EM structure of the DNA-dependent protein kinase catalytic subunit at subnanometer resolution reveals alpha helices and insight into DNA binding. Structure 16, 468–477.

Williams, G.J., Hammel, M., Radhakrishnan, S.K., Ramsden, D., Lees-Miller, S.P., Tainer, J.A., 2014. Structural insights into NHEJ: building up an integrated picture of the dynamic DSB repair super complex, one component and interaction at a time. DNA Repair (Amst) 17, 110–120.

Yang, H., Jiang, X., Li, B., Yang, H.J., Miller, M., Yang, A., et al., 2017. Mechanisms of mTORC1 activation by RHEB and inhibition by PRAS40. Nature 552, 368–373.

Yano, K., Chen, D.J., 2008. Live cell imaging of XLF and XRCC4 reveals a novel view of protein assembly in the non-homologous end-joining pathway. Cell Cycle (Georgetown, Tex) 7, 1321–1325.

Yin, X., Liu, M., Tian, Y., Wang, J., Xu, Y., 2017. Cryo-EM structure of human DNA-PK holoenzyme. Cell Res. 27, 1341–1350.

Yoo, S., Dynan, W.S., 1999. Geometry of a complex formed by double strand break repair proteins at a single DNA end: recruitment of DNA-PKcs induces inward translocation of Ku protein. Nucleic Acids Res. 27, 4679–4686.

Zhou, Y., Millott, R., Kim, H.J., Peng, S., Edwards, R.A., Skene-Arnold, T., et al., 2019. Flexible tethering of ASPP proteins facilitates PP-1c catalysis. Structure 27, 1485–1496.